Journal of Instrumentation

SISSA

OPEN ACCESS

Measurement of beam-correlated background neutrons from the Fermilab Booster Neutrino Beam in ANNIE Phase-I

To cite this article: A.R. Back *et al* 2020 *JINST* **15** P03011

Published by IOP Publishing for Sissa Medialab

Received: *December 6, 2019*
Accepted: *February 7, 2020*
Published: *March 17, 2020*

Measurement of beam-correlated background neutrons from the Fermilab Booster Neutrino Beam in ANNIE Phase-I

The ANNIE collaboration

A.R. Back,[b] J.F. Beacom,[d] T. Boschi,[c,1] D. Carber,[b] E. Catano-Mur,[b,2] M. Chen,[f,3] E. Drakopoulou,[i] F. Di Lodovico,[c] A. Elagin,[h] J. Eisch,[b] V. Fischer,[f] S. Gardiner,[f,4] J. Griskevich,[g] D. Grzan,[b,5] R. Hatcher,[a] F. Krennrich,[b] B. Kimmelman,[f] A. Kreymer,[a] W. Lee,[a,6] S. Locke,[g] M. Long,[f] M. Malek,[j] C. McGivern,[a] E. Moore,[f] M. Needham,[i] M. O'Flaherty,[j] J. Podczerwinski,[b,7] B. Richards,[k] J. Ritz,[g] M. C. Sanchez,[b] M. Smy,[g] R. Svoboda,[f] E. Tiras,[b] M. Vagins,[g] J. Wang,[f] P. Weatherly,[g,8] A. Weinstein,[b] M. Wetstein[b,*] and J. Wu[b]

[a] *Fermi National Accelerator Laboratory, Batavia, IL 60510, U.S.A.*
[b] *Iowa State University, Ames, IA 50011, U.S.A.*
[c] *Kings College London, London WC2R2LS, U.K.*
[d] *Ohio State University, Columbus, OH 43210, U.S.A.*
[e] *Queen Mary University of London, London E14NS, U.K.*
[f] *University of California, Davis, Davis, CA 95817, U.S.A.*
[g] *University of California, Irvine, Irvine, CA 92697, U.S.A.*
[h] *University of Chicago, Enrico Fermi Institute, Chicago, IL 60637, U.S.A.*
[i] *University of Edinburgh, Edinburgh EH9 3FD, U.K.*
[j] *University of Sheffield, Sheffield S10 2TN, U.K.*
[k] *University of Warwick, Coventry CV47AL, U.K.*

E-mail: wetstein@iastate.edu

[1] Present address: Queen Mary University of London; London, E14NS, U.K. .
[2] Present address: College of William & Mary; Williamsburg, VA 23187, U.S.A. .
[3] Present address: Lehigh University; Bethlehem PA 18015, U.S.A. .
[4] Present address: Fermi National Accelerator Laboratory; Batavia, IL 60510, U.S.A. .
[5] Present address: University of California, Davis; Davis, CA 95817, U.S.A. .
[6] Deceased.
[7] Present address: University of Wisconsin; Madison, WI 53708, U.S.A. .
[8] Present address: Drexel University; Philadelphia PA 19104, U.S.A. .
[*] Corresponding author.

https://doi.org/10.1088/1748-0221/15/03/P03011

Abstract: The Accelerator Neutrino Neutron Interaction Experiment (ANNIE) aims to make a unique measurement of neutron yield from neutrino-nucleus interactions and to perform R&D for the next generation of water-based neutrino detectors. In this paper, we characterize beam-induced neutron backgrounds in the experimental hall at Fermi National Accelerator Laboratory. It is shown that the background levels are sufficiently low to allow the next stage of the experiment to proceed. These measurements are relevant to other Booster Neutrino Beam (BNB) [1] experiments located adjacent to ANNIE Hall, where dirt neutrons and sky-shine could present similar backgrounds.

Keywords: Cherenkov detectors; Neutrino detectors; Neutron detectors (cold, thermal, fast neutrons); Particle identification methods

ArXiv ePrint: 1912.03186

2020 JINST 15 P03011

Contents

1 Introduction **1**

2 Experimental design of the neutron background measurement **4**
- 2.1 Neutron Capture Volume (NCV) 4
- 2.2 Upstream and downstream veto and muon selection 5
- 2.3 Electronics, trigger, and data acquisition system 5

3 Data taking and selection **6**

4 Signal processing **7**
- 4.1 Pedestal estimation 7
- 4.2 Pulse finding 8
- 4.3 Waveform calibration 8
- 4.4 Feature extraction 8

5 Neutron candidate selection **8**
- 5.1 NCV coincidence requirement 10
- 5.2 After-pulsing requirement 10
- 5.3 Total charge cut 10
- 5.4 Water PMT veto cut 11

6 Calibration measurements **11**
- 6.1 Arrival time distribution of detected neutrons from a ^{252}Cf source 12
- 6.2 NCV neutron detection threshold measurement using cosmic muon data 12
  - 6.2.1 Charge threshold measurement 12
  - 6.2.2 Energy scale calibration 12
  - 6.2.3 Calculation of the NCV neutron detection threshold 13

7 Estimation of the NCV efficiency **13**
- 7.1 Measuring the NCV efficiency with a ^{252}Cf source 14
- 7.2 Estimating the NCV efficiency using the neutron detection threshold 15

8 Computing the beam-induced neutron event count **16**
- 8.1 Subtraction of the constant-in-time (CIT) background 16
  - 8.1.1 CIT background estimation using pre-beam data 17
  - 8.1.2 CIT background estimation using late-time data 17
- 8.2 After-pulsing correction 18
- 8.3 Beam-correlated neutron event counts 18

9 Computing the beam-induced neutron event rate **19**

2020 JINST 15 P03011

10 Systematic uncertainties in the beam-induced neutron event rate **20**
10.1 Systematic uncertainties on N_n 20
10.2 Measurement of ϵ_{NCV} and associated systematic error 21
10.3 Systematic uncertainties in exposure and volume scaling 21
10.4 Combined uncertainty estimate 21

11 Implications for the ANNIE neutron multiplicity measurement **21**

12 Conclusions **24**

2020 JINST 15 P03011

1 Introduction

The Accelerator Neutrino Neutron Interaction Experiment (ANNIE) [2] aims to make the first detailed measurement of the number of neutrons produced by muon neutrinos interacting with nuclei. Measurements of the final-state neutron multiplicity are key to improving our understanding of neutrino-nucleus interactions. This in turn improves our understanding of systematic uncertainties in neutrino oscillation experiments, where the energy carried by difficult-to-detect final-state neutrons can degrade the resolution of the reconstructed neutrino energy. Identifying and counting final-state neutrons also provides a new and critical handle on signal-background separation in future proton decay and neutrino experiments [3].

The lower panel of figure 1 shows the detector configuration (referred to as Phase-II) used to perform the final-state neutron multiplicity measurement. The main target consists of an upright cylindrical steel tank filled with 26 metric tons of gadolinium-loaded (Gd-loaded) ultra-pure deionized water, instrumented with photodetectors and partially enclosed by a muon detection system. A muon produced by a neutrino interaction in the fiducial volume is reconstructed using the tank photodetectors and the muon detection system. Neutrons produced by the neutrino interaction scatter and lose energy through thermalization, allowing them to capture on either H or Gd in the active volume. The fall-off in the neutron capture cross-section with energy for both pure and Gd-loaded water is shown in figure 2. Gd-loading dramatically enhances the cross-section relative to pure water for energies near and below the thermal neutron energy of 0.025 eV. The capture produces a delayed signal in the form of a de-excitation γ-ray cascade, with properties determined by the capturing nuclide. In particular, captures on Gd produce a more easily-detected ~8 MeV γ-ray cascade compared with the 2.2 MeV cascade from H-capture. At concentrations of 0.1% Gd by mass, the enhanced cross-section has the added benefit of shortening the time constant for neutron capture from ~200 µs to ~30 µs. These combined effects make Gd-loading essential to the final-state neutron multiplicity measurement.

Because final-state neutrons in ANNIE can travel over a meter before thermalizing and capturing in the ~14 m^3 ANNIE active volume, neutrino-induced neutrons and background neutrons are spatially indistinguishable. As a consequence, any neutrons entering the tank that are unrelated to the neutrino interaction constitute a potential background for the ANNIE physics program. Restricting the analysis to a narrow time window around the arrival of the neutrino beam spill

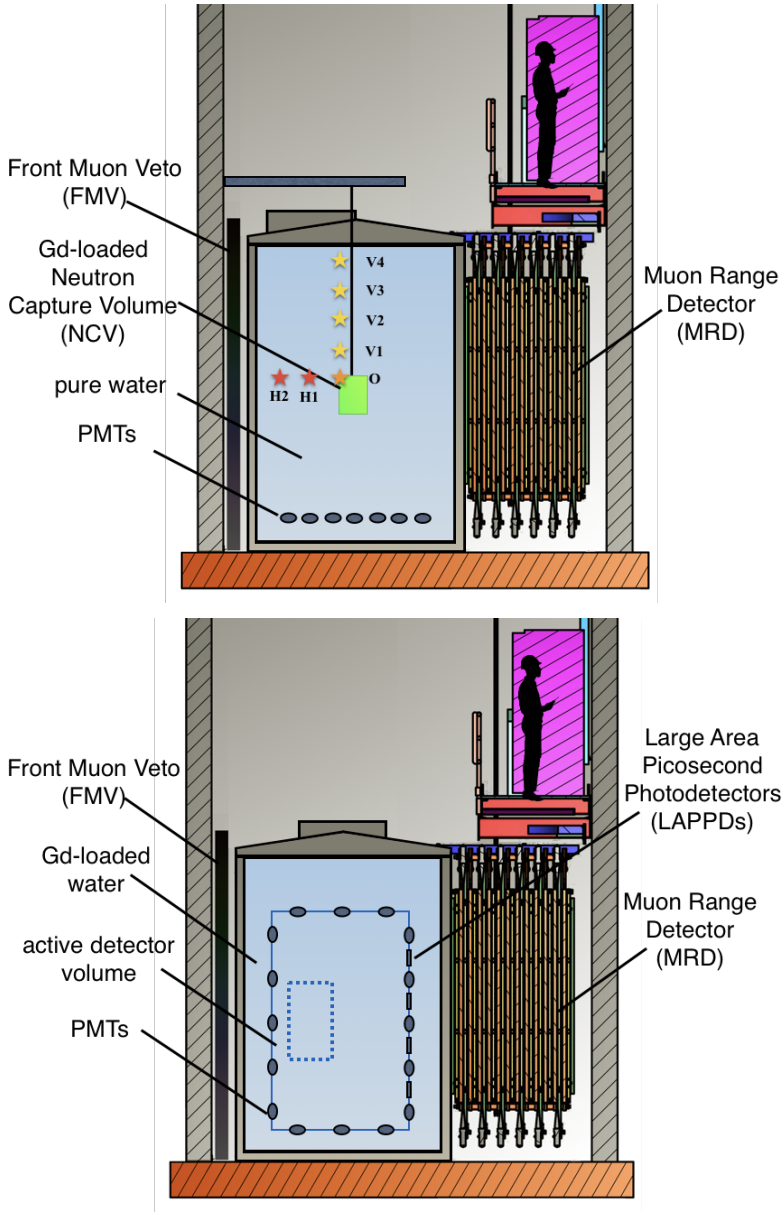

Figure 1. TOP: a concept drawing of the Phase-I ANNIE detector system, showing the positions of the upper left corner of the neutron capture volume (NCV) described in section 2. BOTTOM: a concept drawing of the complete Phase-II detector. The solid blue line indicates the optically isolated active volume of the detector and the dotted blue line indicates the fiducial volume optimized for the Phase-II physics measurement.

suppresses a large fraction of the constant-in-time (CIT) background activity arising from processes unrelated to the beam. The residual CIT background can be characterized by taking off-beam triggers. All remaining backgrounds are correlated in time with the beam.

There are two dominant types of beam-correlated neutron backgrounds, both of which are delayed relative to the prompt component from beam neutrino interactions. The first type, referred to as *sky-shine*, consists of secondary neutrons produced in the beam dump that leak into the

2020 JINST 15 P03011

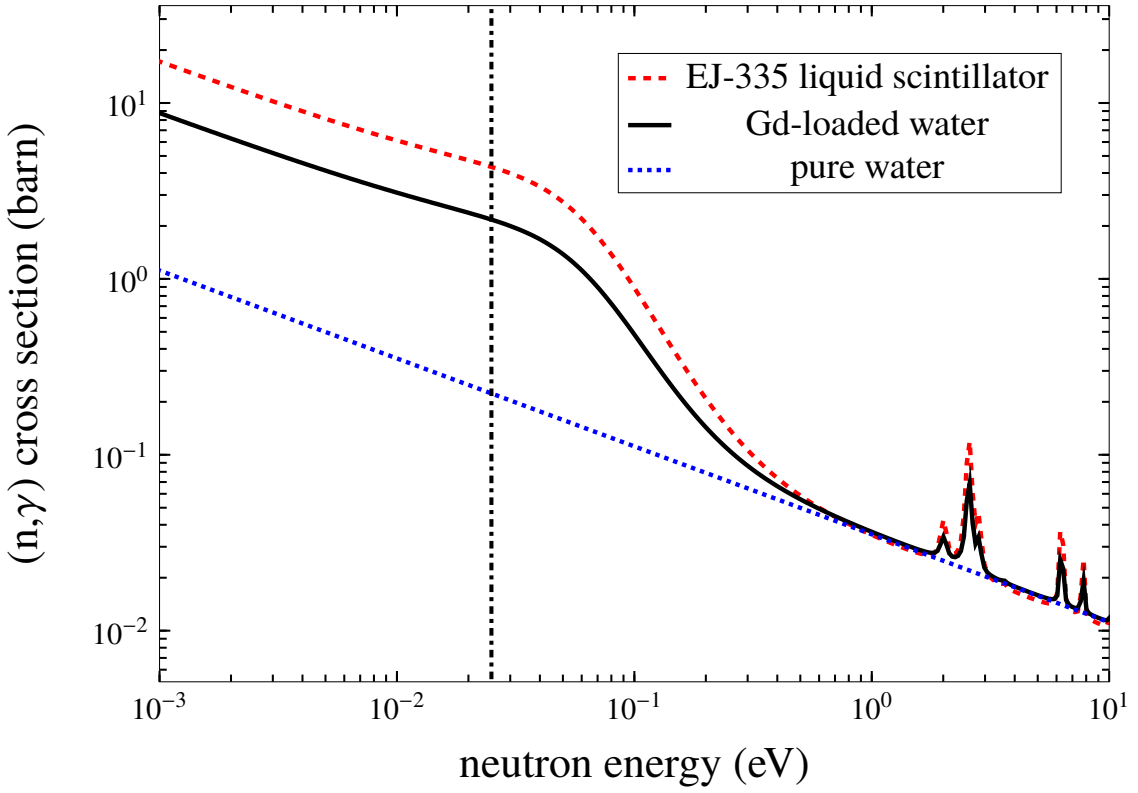

Figure 2. The neutron capture cross section as a function of energy for pure water, EJ-335 Gd-loaded liquid scintillator (0.25% w/w), and the Gd-loaded water (0.1% w/w) to be used in ANNIE Phase-II. The results shown in the plot, which are weighted by nuclide fraction, were computed using cross sections for pure nuclides taken from ENDF/B-VIII.0 [7]. The dash-dotted vertical line at 0.025 eV indicates a typical kinetic energy for a thermal neutron.

atmosphere and enter the detector after undergoing multiple scattering [4, 5]. Preliminary results from the SciBooNE experiment, which previously occupied the ANNIE experimental hall, show an excess of presumed sky-shine events after the beam spill with a clear dependence on detector depth [6]. The dependence of the event count with respect to depth suggests that using a fiducial volume away from the top of the detector would significantly reduce the sky-shine background. The second type of background, known as *dirt neutrons*, consists of neutrons that arise from beam neutrino interactions occurring in the dirt and rock upstream of the experimental hall. The optically isolated buffer region of water upstream of the ANNIE Phase-II active volume should reduce the dirt neutron flux.

In this paper, we report a first measurement of beam-correlated background neutrons in the ANNIE tank as a function of position. This analysis uses data taken in a special configuration (ANNIE Phase-I) of the detector with a pure water target. This configuration is pictured schematically in the upper panel of figure 1. We measure a rapid fall-off of the neutron background with depth and demonstrate that neutron backgrounds in the detector volume are limited. We also use the measured fall-off as a function of distance from the surface of the water and the tank walls in Phase-I to verify that the proposed buffer region surrounding the optically isolated volume for the

2020 JINST 15 P03011

main ANNIE neutrino interaction physics program, known as Phase-II (lower panel of figure 1), provides adequate shielding from background neutrons. As the size of this buffer region could only be increased by reducing the size of the optically isolated volume, this indicates that we can achieve the necessary background levels while accommodating a neutrino vertex fiducial volume large enough (~2.5 m^3) to contain the neutrons from neutrino interactions. These results establish the feasibility of the Phase-II physics program.

The measurements presented in this paper are relevant to other Booster Neutrino Beam (BNB) [1] experiments such as the Short Baseline Near Detector (SBND), located adjacent to ANNIE Hall, where dirt neutrons and sky-shine could present similar backgrounds. The techniques described in this paper will also be applicable to any future water-based near detectors, especially those with Gd-loading or water-based liquid scintillators.

2 Experimental design of the neutron background measurement

The ANNIE detector is installed in the BNB at Fermilab at the former location of the SciBooNE [8] detector. The BNB runs at an average rate of 5 Hz. Protons are delivered in 84 bunches over a 1.6 µs spill time to a target and horn combination 100 m upstream of ANNIE Hall. The nominal number of protons-on-target (POT) per spill is 5×10^{12} POT. The beam is estimated to produce 93% pure ν_μ, with an energy spectrum peaking at around 700 MeV [9]. At the location of the detector, the neutrino beam width is comparable to the size of the ANNIE tank itself, providing an approximately uniform illumination of the full water volume. Neutrino interactions in the tank are expected to occur in about 1% of beam spills, with approximately two-thirds of these being charged-current.

The ANNIE Phase-I neutrino target and optical instrumentation (shown in figure 1) were contained in a steel tank roughly 3 m in diameter by 4 m in height. The interior of the tank was covered with a white reflective PVC liner in order to maximize light collection and was filled with 26 metric tons of ultra-pure deionized water. An array of 58 upward-facing 8-inch Hamamatsu R5912 photomultiplier tubes (PMTs) was installed inside the water volume at the base of the tank. All of these PMTs were mounted on an octagonal, stainless-steel inner structure that, along with the attached tank lid, could be lifted out and replaced without moving the tank itself. A set of six plastic scintillator paddles, each with an attached light guide and a 2-inch PMT, was mounted in a metal frame placed on top of the tank lid. These paddles were used to generate triggers on directionally-selected cosmic muons.

2.1 Neutron Capture Volume (NCV)

The position dependence of beam-correlated neutron backgrounds is characterized using a movable Neutron Capture Volume (NCV) deployed within the tank. The NCV is a 50 cm × 50 cm acrylic cylinder filled with EJ-335, a Gd-loaded (0.25% w/w) liquid scintillator manufactured by Eljen Technology [10]. Thermal neutron capture on Gd produces a γ-ray cascade with a total energy of around 8 MeV, which is detectable as a bright flash of light in the scintillator. The radiation length in the NCV is roughly 50 cm, and thus neutron capture γ-rays are often not fully contained, limiting the detection efficiency of the volume to around 10% (see section 7). The NCV is moved within the water volume using a sliding winch. A slot on the hatch of the tank lid permits translation of the NCV in the beam direction. All of the data used in this paper were taken in a mode where the NCV

2020 JINST 15 P03011

was wrapped in successive layers of reflective white plastic to maximize total internal reflection and black plastic to optically isolate it from the rest of the tank. Two 3-inch PMTs were installed on top of the NCV in order to tag energy depositions in the liquid scintillator.

2.2 Upstream and downstream veto and muon selection

A front muon veto (FMV) consisting of two layers of overlapping scintillator paddles (originally used by the CDF experiment [11]) sits between the tank and the beam. The FMV is used to reject charged particles produced in the dirt and rock upstream of the detector. A muon range detector (MRD) consisting of 11 alternating layers of iron absorber and vertical and horizontal plastic scintillator paddles (previously used by SciBooNE [12]) sits downstream from the neutrino target. For Phase-I, only two layers were instrumented, which was sufficient to tag outgoing muons. From simulation studies using the GENIE generator [13], it is estimated there are approximately 26,000 charged-current muon neutrino interactions within the ~2.5 m^3 fiducial volume per year, of which roughly 5,000 produce muons that enter and range-out in the MRD.

2.3 Electronics, trigger, and data acquisition system

The detector electronics readout system consists of three subsystems. A Central Trigger Card (CTC) provides synchronization, time-stamping and event tagging. A VME-based system, originally designed for the K0TO experiment [14], digitizes the full waveforms from all of the water PMTs and NCV PMTs at 500 MSamples/sec into a deep buffer capable of recording up to 80 µs. The VME system is also responsible for generating the triggers from the NCV and water PMTs. Finally, a CAMAC-based TDC system time stamps and records pulses above threshold from the FMV and the MRD.

These systems are integrated using the data acquisition (DAQ) framework ANNIEDAQ [15], a modular and scalable DAQ framework based on ToolDAQ [16]. The software runs in a distributed way on multiple servers and the VME computer cards. It is responsible for run and high voltage control, slow-control monitoring, maintaining the run status database, trigger mode configuration, and managing data from each of the asynchronously-running detector subsystems (FMV, water and NCV PMTs, and the MRD). The electronics and DAQ software are highly scalable and configurable and will serve as the baseline for the ANNIE Phase-II detector.

All trigger signals are managed by the configurable CTC, a CAEN V1495 general purpose VME board with ECL and LVDS inputs and a customizable FPGA. The CTC receives a signal from the BNB facility that provides advance notification of a beam spill arriving (beam trigger) and forwards appropriately time-delayed copies to the VME and CAMAC systems. The CTC also passes through and timestamps a Global Positioning System (GPS) 1PPS signal, used for synchronization.

Data taking occurred in two different trigger modes. These two modes are depicted in figure 3. Mode A records the waveforms for all channels for an 80 µs time window, large enough to include all prompt activity and the majority of subsequent neutron captures. In this mode, data are recorded in response to a beam trigger without imposing any requirement on PMT activity in the NCV or water tank. The start of the beam trigger is placed 10 µs into the 80 µs buffer, providing a high statistics sample of the pre-beam random background. This mode has the advantage of being insensitive to the detection threshold for neutron captures. In Mode B, data are recorded unconditionally from all

2020 JINST 15 P03011

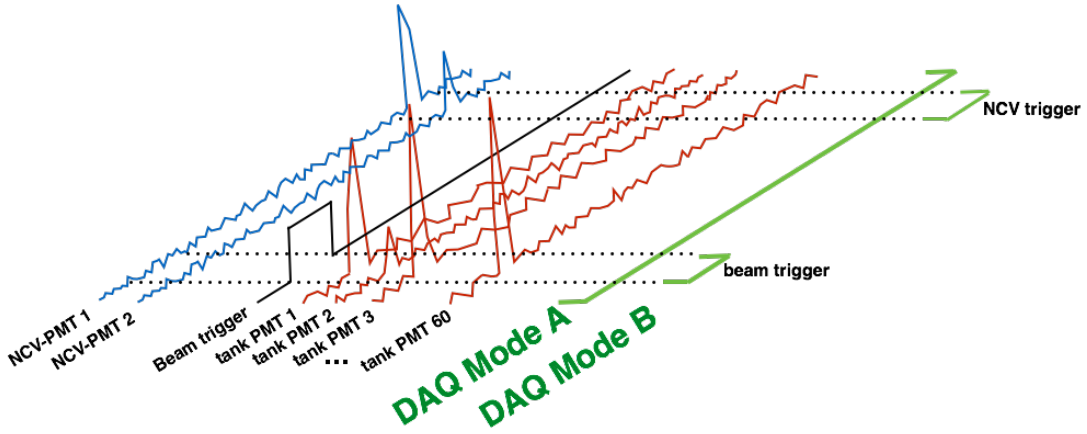

Figure 3. A cartoon representation showing how a digitized ANNIE event is recorded in the two different DAQ modes.

channels during a 2 µs window around the beam trigger. Additional 2 µs recordings of all channels are stored for any NCV triggers (defined as either of the two NCV PMT signals exceeding a hardware threshold of 357 ADC counts) within a 100 µs gate following the beam trigger. The value of the Mode B hardware threshold was chosen to be as low as possible while maintaining a manageable data rate for the DAQ electronics. An onboard 64-bit counter, calibrated using synchronization pulses from the central trigger card and the VME CPU UTC time, permits offline correlation of all ADC records associated with a Mode B trigger. This mode reduced deadtime while requiring a more sophisticated understanding of the relationship between neutron captures and trigger thresholds. It also required the adoption of pre-scaled off-beam triggers.

Neutron thermalization happens rapidly (within a few µs) in water and scintillator. The 12 µs time constant for capture of thermal neutrons in EJ-335 liquid scintillator is therefore the primary consideration needed to select a suitable time window for neutron detection in ANNIE Phase-I. Both DAQ modes described above were designed to allow neutron captures to be recorded over a time period spanning several time constants.

3 Data taking and selection

The beam data used in this paper were collected from February through August of 2017, representing a total exposure of 6.24×10^{19} POT. Data were collected with the NCV at seven different positions, shown in the top panel of figure 1 and using a mix of the two DAQ modes described in section 2.3. The NCV positions are numbered with respect to a reference position (position O) at the center of the tank. The H positions are numbered to increase with decreasing horizontal shielding. The V positions are numbered to increase with decreasing water overburden. An uncertainty of 2 cm was estimated for all NCV position measurements.

All beam data at position V4 were taken in DAQ mode A. All data at positions V1–3 and H1–2 were taken in DAQ mode B. At position O, located in the center of the tank, total exposures of 3.57×10^{18} POT (875,867 beam spills) and 1.409×10^{19} POT (3,692,460 beam spills) were obtained in DAQ modes A and B, respectively. The measured rates were consistent within one-sigma uncer-

2020 JINST 15 P03011

Table 1. Summary of the data collected during ANNIE Phase-I.

NCV position	Water overburden[a] (cm)	Water shielding[b] (cm)	Beam spills	Total exposure (10^{18} POT)	Average POT per spill (10^{12} POT)	Cosmic triggers
O	138 ± 2	104 ± 2	4,568,327	17.66	3.87	33,437
H1	138 ± 2	58 ± 2	650,378	2.20	3.39	6,575
H2	138 ± 2	10 ± 2	4,383,135	13.24	3.02	40,451
V1	67 ± 2	104 ± 2	2,023,082	6.79	3.36	26,610
V2	36 ± 2	104 ± 2	3,476,203	10.98	3.16	59,387
V3	21 ± 2	104 ± 2	973,057	3.63	3.73	11,502
V4	6 ± 2	104 ± 2	1,779,098	7.88	4.43	17,217

[a]The thickness of water above the NCV.
[b]The thickness of water between the beam-side wall of the tank and the NCV.

tainties between the two approaches. In addition to the data in table 1, six ^{252}Cf source calibration runs were performed with the NCV at position V4, providing a total of 206,732 source triggers.

Table 1 summarizes the number of beam spills, total exposure, and total number of cosmic muon triggers recorded at each position.

4 Signal processing

The Phase-I data were processed and analyzed using ToolAnalysis [17], an event reconstruction software package developed by ANNIE collaborators within the ToolDAQ framework [16]. All of the information used in neutron candidate reconstruction and selection is derived from PMTs attached to the NCV and the bottom of the tank. In this section we describe the PMT signal processing.

4.1 Pedestal estimation

The pedestal ADC value for each PMT channel, denoted x_0, is estimated according to the ZE3RA algorithm [18]. To apply this algorithm, 40 time slices, each 25 ADC samples long, are chosen from regions of data that are expected to be pulse-free. For Mode A, the 40 time slices are contiguous and correspond to the first 2 µs of the full 80-µs readout window. For Mode B, the time slices are obtained from the first 50 ns of 40 consecutive 2-µs data records.

The mean and variance of the 25 ADC values in each time slice are calculated, and the sample variances of neighbouring slices are checked for statistical consistency using an F-test. Time slices that are identified as inconsistent, likely due to the presence of nuisance pulses or electrical transients, are flagged and removed. The pedestal x_0 is then taken to be the mean of all ADC values from the remaining slices. The standard deviation σ_{x_0} of the ADC samples selected in this way is used in PMT pulse finding. The values of x_0 and σ_{x_0} are recalculated for each readout window to account for slow variations of the pedestal over time.

2020 JINST 15 P03011

4.2 Pulse finding

With the exception of a 2 µs time window immediately around the beam trigger, Mode B imposes a hardware threshold on the NCV PMTs for recording data. This is in contrast to Mode A, which records a full 80 µs of data in response to a beam trigger without any threshold requirement. To ensure consistency between Mode A and Mode B, pulse finding is performed prior to pedestal subtraction and calibration for each PMT channel. Starting with the first digital sample in a waveform, ADC values are sequentially checked until the appropriate pulse finding threshold is exceeded. This corresponds to 357 ADC counts for the NCV PMTs (chosen to match the Mode B hardware threshold, see section 2.3) and 7 ADC counts above pedestal for the tank PMTs (chosen to achieve good muon rejection using the "water PMT veto cut" described in section 5.4). The first digital sample for which this occurs is defined as the beginning of a pulse. The subsequent samples are checked until one of the following conditions is met: (1) an ADC value is found that falls below $x_0 + \sigma_{x_0}$, or (2) the end of the record is reached. The digital sample fulfilling the logical OR of these criteria is defined to be the end of the pulse.

4.3 Waveform calibration

After subtracting the pedestal, the ADC waveforms are calibrated. For the ANNIE ADC cards, the voltage V_{PMT} corresponding to a recorded ADC value x_{ADC} is given by the relation:

$$V_{\mathrm{PMT}} = \frac{2.415\ \mathrm{V}}{2^{12}\ \mathrm{ADC\ counts}} (x_{\mathrm{ADC}} - x_0). \tag{4.1}$$

Calibrated waveforms are obtained by applying the conversion formula eq. (4.1) to each of the raw samples.

4.4 Feature extraction

The fully calibrated pulses are characterized using the following feature-extraction parameters: (1) start time: the starting sample index multiplied by the sampling period; (2) peak time: the time at which the maximum ADC value occurred within the pulse (If the maximum ADC value was reached more than once during the pulse, then the earliest sample for which this occurred is used to calculate the peak time); (3) end time: the time corresponding to the first sample after the start of the pulse at which either the ADC signal fell below $x_0 + \sigma_{x_0}$ or the data record ended; (4) raw amplitude: the maximum ADC value recorded during the pulse; (5) calibrated amplitude: the maximum voltage recorded during the pulse, calculated using eq. (4.1) with x_{ADC} set equal to the raw amplitude of the pulse; and (6) charge: the time integral of the calibrated version of the pulse divided by the ADC input impedance (50 Ω).

5 Neutron candidate selection

Neutrons are identified by a burst of scintillation light detected within the NCV over a time region of interest between 10 µs and 70 µs after the beam arrival. Events are selected that have no prompt neutrino interaction in the tank but that have a delayed signal consistent with the capture of neutrons entering from outside the detector volume. The compact size of the NCV provides localization of

2020 JINST 15 P03011

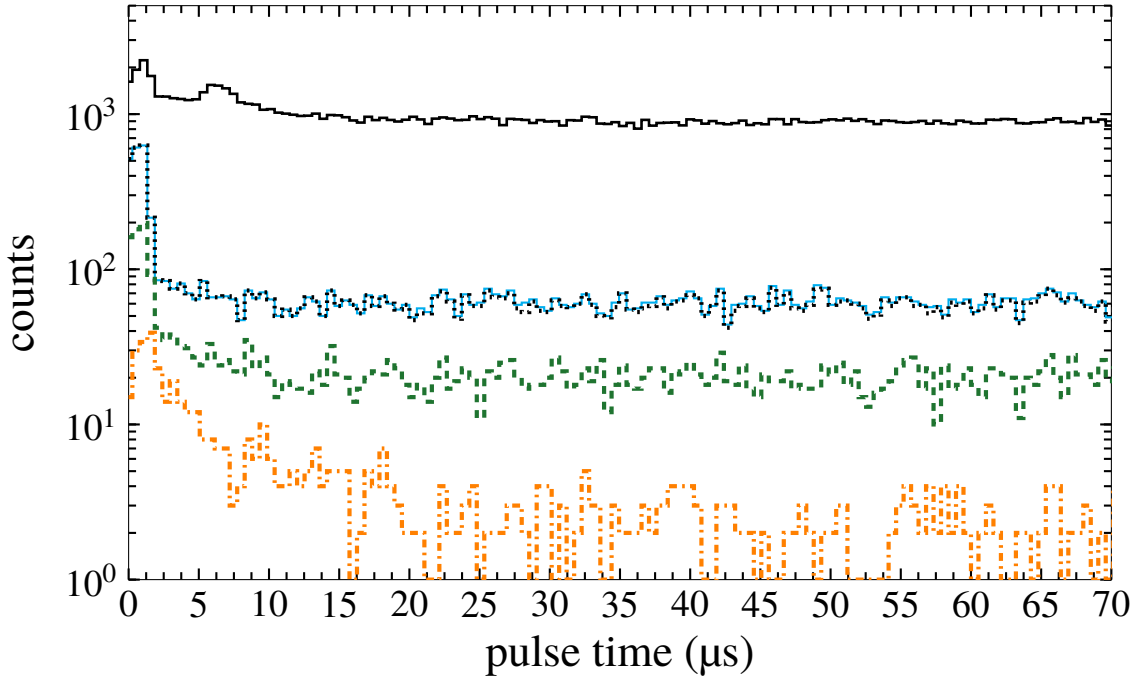

Figure 4. Successive applications of each of the neutron candidate event criteria for beam data taken at position O (center of the tank). SOLID BLACK: time distribution of all pulses recorded in DAQ Mode B on NCV PMT #1 at position O. A time of zero corresponds to beam arrival. No analysis cuts have been applied to these data. SOLID CYAN: time distribution of all NCV coincidences from the same dataset. DOTTED BLACK: events from the blue histogram that passed the after-pulsing cut. Note that this cut was not applied to events that occurred in the first 20 μs after the start of the beam spill. DASHED GREEN: events from the red histogram that passed the total charge cut. DASH-DOTTED ORANGE: events from the green histogram that passed the water PMT veto cut.

the neutrons. The quantity and spread of the light detected on the PMTs at the bottom of the water volume are used to veto cosmic muons. The count of neutrons detected in the NCV is divided by the beam exposure and NCV volume to determine the rate of background neutrons per unit volume per beam spill.

The solid black curve in figure 4 shows the time distribution (relative to the start of the beam spill) for all of the reconstructed pulses found on one NCV PMT (#1) during beam data taking in Mode B at NCV position O (the center of the tank). Three features of the distribution are immediately apparent. The first is a dominant flat component composed primarily of dark pulses with a contribution from cosmic-ray muons. The second is a peak synchronous with beam arrival. This corresponds primarily to beam neutrino interactions in the tank, with an admixture of beam-induced muons. A later peak, attributable to a combination of fast neutron scatters and after-pulsing, appears roughly 5 μs after the first.

Rather than relying on simulations to estimate efficiencies for individual analysis cuts, we measure the combined efficiency from all cuts folded with the acceptance of the NCV, as described in section 7. Thus any cut efficiencies and purities described in this section are provided solely for heuristic purposes and have not been used directly in the final measurement.

2020 JINST 15 P03011

5.1 NCV coincidence requirement

To reduce the number of spurious events due to dark noise and after-pulsing, neutron capture candidates were selected by requiring two pulses, one from each NCV PMT, whose start times (calculated as described in section 4.2) fell within a 40-ns coincidence window. The earlier start time is designated as the time of the event. The solid cyan curve in figure 4 shows the time distribution of neutron candidates remaining after the NCV coincidence requirement is applied. While the beam-correlated peak at $t = 0$ µs is still present, the second peak at 5 µs has disappeared, as would be expected if it is largely composed of after-pulses on NCV PMT #1.

Given the measured dark rates of the NCV PMTs (476 Hz for PMT #1 and 87 Hz for PMT #2) we estimate the rate of accidental coincidences for our chosen 40-ns coincidence window to be 1.7×10^{-3} Hz. This translates to a negligible contribution of 1.4×10^{-7} counts per spill from accidental NCV coincidences.

5.2 After-pulsing requirement

NCV coincidences due to after-pulsing can be suppressed by requiring that a coincidence occur at least 10 µs after the most recently-accepted neutron candidate. However, it is not possible to distinguish spurious candidates due to after-pulsing and events in which a fast neutron scatters within the NCV shortly before a true neutron capture. Neutrons produced by trace radioisotopes and cosmic-ray spallation constitute a CIT background that was considered in our calibration of the NCV (see section 6). Apart from these, the only important source of fast neutrons that may enter the ANNIE detector is the beam itself. We assume in our definition of the after-pulsing cut that, by 10 µs after the start of the beam spill, any beam-correlated neutrons that are found inside the detector have dropped below the NCV detection threshold for proton recoils. In order to avoid losing signal while still suppressing the majority of after-pulses, the after-pulsing suppression cut is only applied to NCV coincidences recorded between 20–70 µs after beam arrival.

The dotted black histogram in figure 4 shows the small effect of applying the after-pulsing cut to the Position O beam data. Given a low overall probability of producing neutrons and a low probability of two genuine neutron captures occurring within 10 µs, the signal efficiency for this cut is estimated to approach 100% in the time window of interest.

5.3 Total charge cut

To suppress NCV coincidences from cosmic- and beam-induced muons, neutron candidates were eliminated if their energy deposition in the scintillator was well above the maximum of 9 MeV expected from a fully-contained neutron capture γ-ray cascade (see figure 7). Based on the NCV charge-to-energy calibration described in section 7.2, a loose cut of $Q_{\mathrm{max}} = 150$ pC on the maximum total charge on the two NCV PMTs was adopted. This conservative choice, which corresponded to a deposited energy of about 34 MeV (see eq. (6.1) and table 2) minimized signal loss. The dashed green histogram in figure 4 shows the neutron candidates that remain after applying the cut $Q_1 + Q_2 < Q_{\mathrm{max}}$, where Q_1 and Q_2 are the charges collected by NCV PMTs #1 and #2, respectively, to the candidates in the dotted black histogram. Since this cut is more than three times the maximum deposited energy expected from neutron captures, we expect negligible signal loss.

2020 JINST 15 P03011

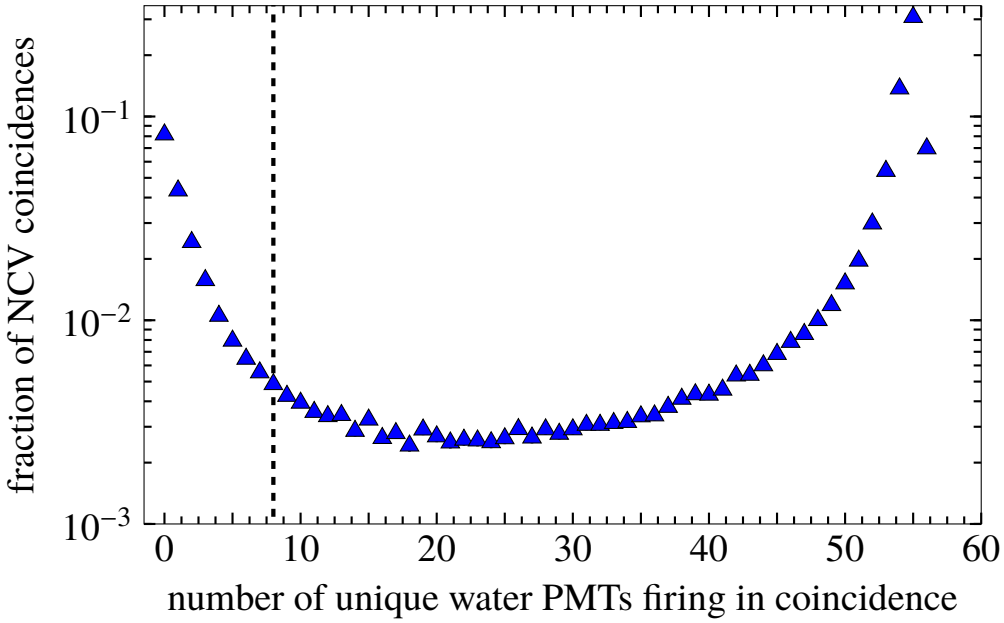

Figure 5. Distributions of the number of unique water tank PMTs that recorded at least one pulse within 40 ns of an NCV coincidence. The data shown here include all runs analyzed for this paper. Events to the right of the dashed vertical line are removed by the water PMT veto cut.

5.4 Water PMT veto cut

Muons that exit the NCV after traveling only a short distance through the scintillator may deposit an energy low enough to pass the NCV total charge cut. The majority of these muons will produce enough light to activate the PMTs at the bottom of the tank. On the other hand, from simulations we calculate that 98% of neutron captures occurring within the NCV produce pulses on 8 or fewer water tank PMTs. Figure 5 shows the number of water tank PMTs that recorded a pulse within 40 ns of an NCV coincidence event (blue triangles). The coincident events show a bimodal distribution in the number of tank PMTs that fired. The peak near zero, corresponding to true neutron captures, drops to within a factor of three of the accidental background at 8 PMTs. The peak near 55 PMTs corresponds to muons traversing the NCV. We veto the latter events by rejecting neutron candidates with more than 8 water tank PMTs firing within 40 ns of the event start time. The resulting pulse time distribution (after applying this and previous cuts) is shown by the dash-dotted orange curve in figure 4.

This cut removes 99.8% of the cosmic-ray calibration sample. Any residual contamination is addressed via the CIT background subtraction in section 8. While this cut is expected to remove prompt activity due to neutrino-induced muons produced in or outside of the tank, subsequent neutron captures (which are delayed with respect to the muon emission) will be preserved.

6 Calibration measurements

Two calibration measurements were performed to estimate the neutron detection efficiency of the NCV. The first of these was a direct measurement of neutrons from a ^{252}Cf fission source. The second was a determination of the energy scale and neutron detection threshold of the NCV using cosmic-ray muons.

2020 JINST 15 P03011

6.1 Arrival time distribution of detected neutrons from a ^{252}Cf source

Californium-252 is a commonly used radioisotope with a half-life of 2.6 years. In 3.1% of its decays, ^{252}Cf undergoes spontaneous fission to produce an average of 3.7675 ± 0.0040 neutrons [19] and 7.98 ± 0.20 γ-rays [20] per fission. Since the fission γ-rays and neutrons are emitted nearly simultaneously, a γ-ray-based trigger provides a clean neutron sample. For our ^{252}Cf source calibration runs, the NCV was placed at position V4 at the top center of the tank. A small dark box containing an LYSO [21] scintillation crystal coupled to a small photomultiplier tube was placed on the tank hatch above the NCV. The output of the PMT observing the LYSO crystal was connected to a discriminator, and the ^{252}Cf source was placed directly above the crystal. Pulses above the discriminator threshold, attributable to fission γ-rays scattering within the crystal, triggered the acquisition of a 80-µs DAQ Mode A readout window with a reduced (2-µs) pre-trigger region.

In order to obtain a useful calibration of the neutron detection efficiency, the CIT background and neutron candidates faked by γ-rays must be separated from the ^{252}Cf fission neutrons. We do this by measuring the time spectrum of all neutron candidates in the ^{252}Cf runs relative to the start of their respective data acquisition window. The structure of the resulting time distribution is shown in figure 6. The prompt γ-rays appear as a sharp spike in the third bin. The broad bump peaking just before 10 µs has an exponential tail whose time constant matches the expected value for thermal neutron captures in the NCV liquid. In section 7.1 we fit simulations-derived models for these components to the neutron candidate time distribution to extract the NCV efficiency.

6.2 NCV neutron detection threshold measurement using cosmic muon data

In addition to the direct measurement of ^{252}Cf fission neutrons described above, we obtained a separate, indirect measurement of the NCV efficiency by estimating its neutron detection threshold.

The neutron event selection criteria (see section 5) used in this analysis impose an amplitude threshold (357 ADC counts) that must be exceeded by both NCV PMTs in coincidence. This amplitude requirement must be translated into a corresponding deposited energy in order to determine the threshold for neutron detection. We perform this translation by first estimating the mean total charge Q_{thresh} collected on the two NCV PMTs at threshold. Cosmic-ray muon data are then compared with simulations to calibrate the energy scale of the NCV and convert Q_{thresh} into an energy threshold.

6.2.1 Charge threshold measurement

To estimate the mean Q_{thresh} of the threshold charge distribution, a Gaussian fit was performed in the vicinity of the peak of the distribution of the total charge (Q_{sum}) collected on the two NCV PMTs for a large sample of NCV coincidence events (at all positions) with $Q_{\text{sum}} < 100$ pC. The after-pulsing cut was applied to events in the sample to avoid biasing the distribution toward an erroneously low mean value. The result of the fit, $Q_{\text{thresh}} = 20.9$ pC, is given in the first row of table 2.

6.2.2 Energy scale calibration

To calibrate the energy scale of the NCV, a sample of 4,841 NCV coincidence events recorded at position O (center of the tank) was analyzed. Each of these events was recorded in response to the ANNIE Phase-I cosmic muon trigger, which selected a specific set of downward going muon tracks

2020 JINST 15 P03011

Table 2. Results of the fits used to estimate the NCV neutron detection threshold.

Parameter	Variable	Best-fit value[a]	Fit χ^2	DOF[b]
Threshold summed NCV PMT charge peak	Q_{thresh}	(20.9 ± 0.3) pC	5.1	14
Downward muon summed NCV PMT charge peak	$Q_{\mu,\text{peak}}$	(400 ± 8) pC	7.7	7
Simulated downward muon energy deposition peak	$E_{\mu,\text{peak}}$	(91.1 ± 0.2) MeV	2.3	6

[a]Parameter errors are statistical only.
[b]Degrees of freedom.

passing nearly directly through the NCV. The peak of the total charge distribution for the two NCV PMTs was estimated using a Gaussian fit. The fit results are shown in the second row of table 2.

A charge-to-energy conversion factor for the NCV was then extracted by comparing the measured peak charge value to the peak deposited energy value obtained from simulations. In these simulations, a cosmic muon event generator originally written for the G4beamline code [22] was adapted for use with the RAT-PAC detector simulation package [23].

Starting locations for each muon track were sampled from a disk high above the ANNIE detector. The initial muon momenta were sampled using an empirical distribution measured using the CAPRICE94 spectrometer [24]. The energy deposited by muon tracks passing through the simulated ANNIE cosmic trigger geometry appropriately were histogrammed and fit with a Gaussian in the vicinity of the peak of the deposited energy distribution ($E_{\mu,\text{peak}}$) at (91.1 ± 0.2) MeV.

6.2.3 Calculation of the NCV neutron detection threshold

Assuming that the total charge measured by the NCV PMTs is approximately a linear function of the energy deposited in the liquid scintillator, the NCV neutron detection threshold E_{thresh} may be expressed in the form

$$E_{\text{thresh}} = Q_{\text{thresh}} \frac{E_{\mu,\text{peak}}}{Q_{\mu,\text{peak}}} \tag{6.1}$$

where Q_{thresh} is the summed charge on the NCV PMTs at threshold, and the ratio $E_{\mu,\text{peak}}/Q_{\mu,\text{peak}}$ is used as a charge-to-energy conversion factor.

Plugging the best-fit parameter values from table 2 into eq. (6.1) yields the NCV energy threshold $E_{\text{thresh}} = 4.76 \pm 0.12_{\text{stat}}$ MeV. The statistical error given here was propagated analytically from the fit results assuming that all three parameters are independent.

7 Estimation of the NCV efficiency

The NCV efficiency (i.e., the fraction of true neutron captures within the NCV that are actually detected) is estimated using two distinct techniques. The first technique relies on a direct measurement of detected neutrons from the ^{252}Cf fission source. The second is an indirect estimate based on the neutron detection threshold of the NCV, as calibrated using through-going cosmic muons.

2020 JINST 15 P03011

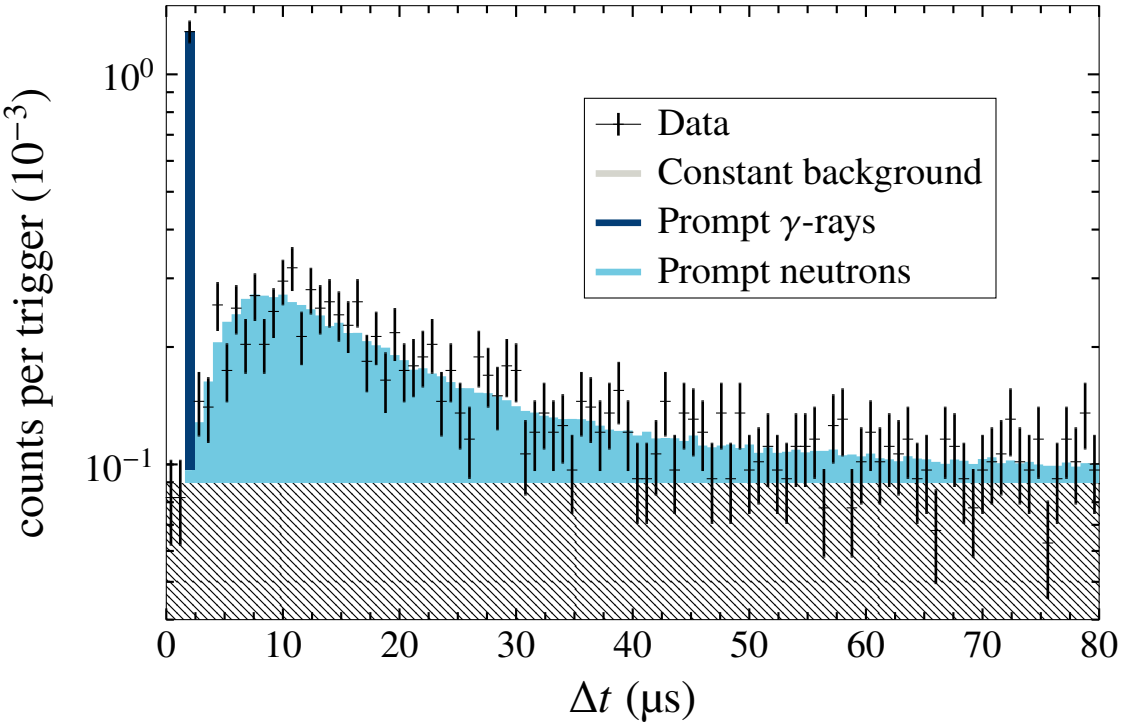

Figure 6. Comparison of the ^{252}Cf calibration source data with the result of a maximum likelihood fit of the model defined in eq. (7.2). The fitted contributions of the constant-in-time background, prompt fission γ-rays, and prompt neutrons from the source are shown separately. The horizontal axis gives the time difference between the start of the DAQ Mode A acquisition window and each neutron candidate event.

Both methods rely on simulations to relate the measured quantities to the NCV efficiency. However, they rely on independent calibration datasets and are primarily sensitive to different aspects of the simulation models. We combine the results from the two approaches to obtain the final measured value of the NCV efficiency and its estimated uncertainty (see Section 10.2).

7.1 Measuring the NCV efficiency with a ^{252}Cf source

As noted in section 3 and section 6.1, six ^{252}Cf source calibration runs were performed with the NCV at position V4, providing a total of 206,732 Mode A data acquisition windows taken when the calibration system triggered on a prompt γ-ray from a ^{252}Cf fission. Figure 6 shows the arrival time distribution of neutron candidate events relative to the start of the associated data acquisition window. This distribution includes three components: a prompt flash from fission γ-rays interacting in the NCV (shown in dark blue), a flat, CIT component (shown in gray), and an excess following the γ flash with a characteristic shape due to neutron captures (shown in light blue).

To extract the NCV efficiency, a maximum likelihood fit to the time distribution in figure 6 is performed using the ROOT [25] interface to MINUIT [26]. The fission γ-rays only contribute to a single time bin and are modeled as a single-bin delta function (denoted $\delta_{j,\gamma\text{flash}}$ in eq. (7.2)). The CIT component is assumed to be flat, which is consistent with the pre-flash region of the time spectrum. The shape of the neutron time distribution is taken from ANNIE RAT-PAC detector simulations

2020 JINST 15 P03011

Table 3. Results of the maximum likelihood fit to the ^{252}Cf source calibration data. The uncertainties are statistical.

Parameter	Variable	Best-fit value
NCV efficiency	ϵ_{NCV}	$(9.60 \pm 0.57) \times 10^{-2}$
Background event rate (Hz)	R	$(1.12 \pm 0.04) \times 10^{2}$
γ-ray event probability	P_γ	$(1.19 \pm 0.08) \times 10^{-3}$
Reduced chi-squared statistic	χ^2/ν	0.753

together with version 2.0.3 of the FREYA event generator [27, 28]. The neutron cross sections used in these simulations were taken from version 4.5 of the Geant4 Neutron Data Library [29].

Formally, the log-likelihood is

$$\ln \mathcal{L} = \sum_j d_j \ln f_j - f_j \tag{7.1}$$

with d_j corresponding to the measured number of events in the jth time bin and the expected number of counts in the jth time bin, f_j, given by

$$f_j(\epsilon_{\mathrm{NCV}}, R, P_\gamma) = N_{\mathrm{windows}} \left(\epsilon_{\mathrm{NCV}}\, \alpha_{n,j} + \delta_{j,\gamma\mathrm{flash}}\, P_\gamma + \Delta t_j\, R\right) \tag{7.2}$$

The three fit parameters are the NCV efficiency ϵ_{NCV}, the CIT background rate in Hz (R), and the fraction of fissions that result in a γ-ray detection in the NCV (P_γ). The quantity $\alpha_{n,j}$ represents the neutron acceptance of the NCV, i.e., the probability that a ^{252}Cf fission produces a true neutron capture inside the NCV during the jth time bin. This is derived from the ^{252}Cf source simulations via the formula

$$\alpha_{n,j} = \frac{N_j}{N_{\mathrm{simulated}}}, \tag{7.3}$$

where N_j is the number of simulated captures that occurred in the jth time bin, and $N_{\mathrm{simulated}} = 10^6$ is the number of simulated fissions. N_{windows} and Δt_j are the number of data acquisition windows and the width of a single time bin.

The values of the best-fit parameters are summarized in table 3. The comparison of this fit result to the source calibration data is shown in figure 6. This method results in a measured NCV efficiency of

$$\epsilon_{\mathrm{NCV}} = 9.60 \pm 0.57_{\mathrm{stat}}\%. \tag{7.4}$$

7.2 Estimating the NCV efficiency using the neutron detection threshold

The second method for estimating the NCV efficiency uses simulations to predict the fraction of true neutron captures that deposit energy in the NCV liquid scintillator above the measured detection threshold of 4.76 MeV. The black curve in figure 7 shows the distribution of the total energy deposition within the scintillator for the 70,470 simulated neutron captures that occured in the NCV liquid volume. A negligible number of external neutron captures produced energy deposits in the NCV. The dashed blue line in figure 7 shows the measured neutron detection threshold of the NCV.

2020 JINST 15 P03011

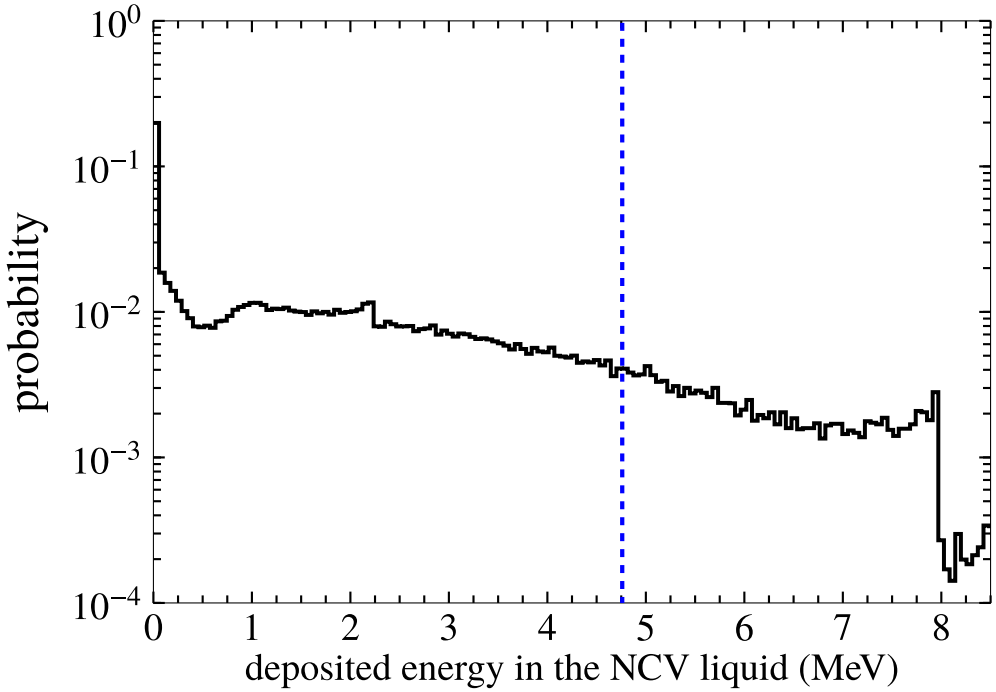

Figure 7. Total energy deposited in the scintillator for simulated neutron captures that occurred within the NCV liquid volume. The estimated NCV neutron detection threshold of 4.76 MeV is indicated by the dashed blue line.

The NCV efficiency, ϵ_{NCV} is the ratio of the simulated NCV capture events with energy depositions above E_{thresh}, divided by the total number of simulated NCV captures:

$$\epsilon_{\mathrm{NCV}} = 12.8 \pm 0.9\,(\mathrm{stat})\%. \tag{7.5}$$

The statistical error shown in eq. (7.5) was found by computing ϵ_{NCV} with the value of E_{thresh} adjusted by a plus or minus one-sigma error.

8 Computing the beam-induced neutron event count

8.1 Subtraction of the constant-in-time (CIT) background

As discussed in section 1, neutron backgrounds for ANNIE's Phase-II physics measurements will consist of a CIT component arising from natural radioactivity and a component correlated in time with spills from the BNB. Because the first of these components can be characterized *in situ* using an off-beam or zero-bias trigger, the goal of ANNIE Phase-I is to isolate and estimate the rate of beam-induced neutron backgrounds in the detector.

We obtain an estimate of the number of beam-induced neutron events at each NCV position by subtracting an estimate of the CIT component from the total count of neutron candidates observed within a 10–70 µs window after the start of each beam spill. With the exception of position V4 (for which a high-statistics measurement of the pre-beam event rate was available), the CIT background at each of the other NCV positions was estimated using two independent techniques.

2020 JINST 15 P03011

The first technique, which relied on pre-beam data taken at position O, provided a value of the CIT event rate which was expected to be an underestimate at other positions. The second technique, which was based on measurements taken at times following the 10–70 µs time region of interest (ROI), provided values expected to be overestimates due to contamination by late captures of beam-correlated neutrons. To mitigate the possible bias introduced by each technique, we adopt a statistically-weighted average of the two values as our estimate of the CIT background event rate (see section 8.3). Our treatment of the systematic uncertainty on the CIT event rates is described in section 10.1.

8.1.1 CIT background estimation using pre-beam data

All of the data collected in position V4 and a portion of the position O data were recorded in DAQ Mode A, where the acquisition time window included 10 µs of pre-beam data. In order to ensure that the sample had no contamination from the beam, the 1 µs prior to beam start is excluded, leaving a total of 9 µs per trigger for estimating the CIT background. We therefore designate the number of events from the first 9 µs of the DAQ Mode A readout window that pass all selection cuts as $N_{\text{pass}}^{\text{pre}}$. Figure 8 shows that the pre-beam event rate is substantially higher at position V4 than with the considerable shielding at position O. For those positions where Mode A data are not available, we used the pre-beam data from the most shielded position (O) to estimate the CIT background.

The general equation for N_n^{pre}, the pre-beam estimate for the number of neutron candidates attributable to CIT background, is

$$N_n^{\text{pre}} = \frac{\Delta t^{\text{ROI}}}{\Delta t^{\text{pre}}} N_{\text{pass}}^{\text{pre}} \frac{\mathcal{T}}{\mathcal{T}_{\text{O}}}. \tag{8.1}$$

Here the scaling factor $\frac{\Delta t^{\text{ROI}}}{\Delta t^{\text{pre}}}$ accounts for the difference in duration of the post-beam region of interest ($\Delta t^{\text{ROI}} = 60$ µs) and the pre-beam region used to estimate the CIT background ($\Delta t^{\text{pre}} = 9$ µs). The measured systematic uncertainty in the time intervals Δt^{ROI} and Δt^{pre} is less than one part in 10^5 and is therefore neglected in this analysis. The factor $\mathcal{T}/\mathcal{T}_{\text{O}}$ is the ratio of recorded beam triggers for the position in question and position O, and is only applicable for the positions where Mode A data are not available.

8.1.2 CIT background estimation using late-time data

At some point after a beam trigger (but before the arrival of a new beam trigger) the event rate should return to baseline. For positions with Mode B data available we had access to neutron candidate events recorded after the signal region of interest and used a period 70–80 µs after beam arrival to obtain a second, independent estimate of the CIT component. We denote the number of events in this time period that pass all selection cuts by $N_{\text{pass}}^{\text{post}}$. The late-time estimate of the number of counts attributable to the CIT background can then be written as

$$N_n^{\text{post}} = \frac{\Delta t^{\text{ROI}}}{\Delta t^{\text{post}}} N_{\text{pass}}^{\text{post}} \tag{8.2}$$

where $\Delta t^{\text{post}} = 10$ µs.

2020 JINST 15 P03011

Table 4. Measurements used to obtain an estimate of the ratio of after-pulses to neutron candidate events $R_{\text{after-pulse}}$.

Signal criteria	Signal events	After-pulses	$R_{\text{after-pulse}}$ (%)
Beam data, mode A, position V4	2,464	10	0.41 ± 0.12
Beam data, mode B, all positions	1,567	13	0.83 ± 0.21
Cf source data, mode A, position V4	1,162	8	0.69 ± 0.22
Weighted mean			0.54 ± 0.09

8.2 After-pulsing correction

As previously noted, the after-pulsing cut is applied uniformly to the pre-beam data but is not applied to neutron candidate pairs in beam data when the first neutron arrives during the initial 10 µs after the beam. Omitting the after-pulsing cut during the initial 10 µs post-beam is intended to prevent accidental suppression of neutron captures that follow shortly after proton recoils induced by fast neutrons. However, inclusion of these events comes at the expense of some contamination by true after-pulses.

In order to correct for this contamination, we calculate the ratio of after-pulses to neutron candidate events by comparing the neutron candidate yield before and after applying the after-pulsing suppression cut. This is done for 40-µs time periods starting 20 µs post-trigger, using both ^{252}Cf calibration data and beam data taken at several positions. The resulting after-pulse rates, with statistical errors, are summarized in table 4. After-pulse-per-neutron rates obtained in the first 10 µs to 20 µs after beam crossing are roughly a factor of two higher, confirming the presence of additional fast neutrons during this time period. We take a weighted average of all results in table 4 to obtain an after-pulse-per-neutron rate of $R_{\text{after-pulse}} = 0.54 \pm 0.09_{\text{stat}}\%$.

8.3 Beam-correlated neutron event counts

The final number of beam-correlated neutron candidate events, corrected for both the CIT background and after-pulsing, is given at any position by

$$N_n = (1 - R_{\text{after-pulse}}) N_n^{10\,\mu\text{s}} + N_n^{\text{later}} - N_n^{\text{CIT}} \tag{8.3}$$

where $N_n^{10\,\mu\text{s}}$ (N_n^{later}) is the raw neutron count in the first 10 µs (remaining 50 µs) of our signal region of interest. The quantity

$$N_n^{\text{CIT}} = \frac{w_{\text{pre}}\, N_n^{\text{pre}} + w_{\text{post}}\, N_n^{\text{post}}}{w_{\text{pre}} + w_{\text{post}}} \tag{8.4}$$

is a weighted average of the two different CIT background estimates where the weights

$$w_{\text{pre}} \equiv \left(N_{\text{pass}}^{\text{pre}}\right)^{-1} \left(\frac{\Delta t^{\text{ROI}}}{\Delta t^{\text{pre}}} \frac{\mathcal{T}}{\mathcal{T}_{\text{O}}}\right)^{-2} \tag{8.5}$$

$$w_{\text{post}} \equiv \left(N_{\text{pass}}^{\text{post}}\right)^{-1} \left(\frac{\Delta t^{\text{ROI}}}{\Delta t^{\text{post}}}\right)^{-2} \tag{8.6}$$

2020 JINST 15 P03011

Table 5. Beam-correlated neutron event rate measurements performed at each NCV position. Columns from left to right: the number of neutron candidate events observed in the time region of interest ($N_n^{\mathrm{ROI}} \equiv N_n^{10\ \mu\mathrm{s}} + N_n^{\mathrm{later}}$), the estimated number of events (N_n^{CIT}) attributable to constant-in-time (CIT) background, the number of events after correcting for the CIT background and after-pulsing (N_n), and the beam-correlated neutron event rate $\mathcal{R}_n^{\mathrm{NCV}}$ per unit volume per beam spill.

NCV position	N_n^{ROI}	N_n^{CIT}	N_n	$\mathcal{R}_n^{\mathrm{NCV}}$ (10^{-2} m^{-3} spill^{-1})
O	339	$333 \pm 45_{\ \mathrm{stat}} \pm 69_{\ \mathrm{syst}}$	$5 \pm 48_{\ \mathrm{stat}}$	$0.013 \pm 0.11_{\ \mathrm{stat}} \pm 0.16_{\ \mathrm{syst}}$
H1	60	$41 \pm 11_{\ \mathrm{stat}} \pm 21_{\ \mathrm{syst}}$	$19 \pm 13_{\ \mathrm{stat}}$	$0.35 \pm 0.24_{\ \mathrm{stat}} \pm 0.40_{\ \mathrm{syst}}$
H2	743	$609 \pm 56_{\ \mathrm{stat}} \pm 192_{\ \mathrm{syst}}$	$133 \pm 62_{\ \mathrm{stat}}$	$0.41 \pm 0.19_{\ \mathrm{stat}} \pm 0.60_{\ \mathrm{syst}}$
V1	254	$206 \pm 30_{\ \mathrm{stat}} \pm 22_{\ \mathrm{syst}}$	$47 \pm 34_{\ \mathrm{stat}}$	$0.29 \pm 0.20_{\ \mathrm{stat}} \pm 0.15_{\ \mathrm{syst}}$
V2	866	$540 \pm 51_{\ \mathrm{stat}} \pm 229_{\ \mathrm{syst}}$	$325 \pm 59_{\ \mathrm{stat}}$	$1.2 \pm 0.23_{\ \mathrm{stat}} \pm 0.9_{\ \mathrm{syst}}$
V3	368	$140 \pm 22_{\ \mathrm{stat}} \pm 124_{\ \mathrm{syst}}$	$227 \pm 29_{\ \mathrm{stat}}$	$2.6 \pm 0.35_{\ \mathrm{stat}} \pm 1.5_{\ \mathrm{syst}}$
V4	3825	$1{,}207 \pm 90_{\ \mathrm{stat}} \pm 0_{\ \mathrm{syst}}$	$2{,}613 \pm 109_{\ \mathrm{stat}}$	$13.6 \pm 0.9_{\ \mathrm{stat}} \pm 3.1_{\ \mathrm{syst}}$

are the reciprocals of the statisical variances from each measurement. The neutron event count results are summarized in table 5. In the third column, the statistical uncertainty on N_n^{CIT} is given by the standard error $(w_{\mathrm{pre}} + w_{\mathrm{post}})^{-1/2}$. At position V4, for which no Mode B data were taken, we use $N_n^{\mathrm{CIT}} = N_n^{\mathrm{pre}}$ with a statistical uncertainty of $w_{\mathrm{pre}}^{-1/2}$.

9 Computing the beam-induced neutron event rate

Figure 8 shows the exposure-normalized neutron candidate event rates as a function of time for NCV positions V4 and O, recorded using DAQ Mode A. Both distributions show a peak in coincidence with the neutrino beam due to prompt activity, distinct from neutron captures. In the center of the tank, a large fraction of the prompt activity likely corresponds to neutrino interactions within the NCV. At the surface, this activity extends a few microseconds after the beam and is likely dominated by fast neutrons scattering off of nuclei in the scintillator.

After removing the CIT background contribution, we can calculate the number of beam-induced neutrons that captured in the NCV by

$$\mathcal{N}_{\mathrm{n}}^{\mathrm{NCV}} = \frac{N_n}{\epsilon_{\mathrm{NCV}}}, \tag{9.1}$$

where N_n is the background-subtracted number of observed neutron candidate events integrated over the time window of interest and ϵ_{NCV} is the NCV efficiency.

The beam-induced neutron event rate (i.e., neutron captures per unit volume per spill) is calculated at each position from

$$\mathcal{R}_n^{\mathrm{NCV}} = \frac{\mathcal{N}_{\mathrm{n}}^{\mathrm{NCV}}}{\mathcal{P}\, V_{\mathrm{NCV}}}, \tag{9.2}$$

where the exposure $\mathcal{P}$ is the total number of POT normalized to nominal spills of 5×10^{12} POT, and V_{NCV} is the volume of the NCV liquid. The results of this calculation, with full statistical and

2020 JINST 15 P03011

Table 6. Constant-in-time (CIT) background event rate estimates at each NCV position. In Mode A, the CIT event rate is estimated using the first 9 µs of each readout window (which precedes the arrival of the beam). In Mode B, the 10 µs following our time region of interest (70–80 µs after beam arrival) is used.

	NCV position	CIT event rate (Hz)
pre-beam (Mode A)	V4	11.4 ± 0.8
	O	1.5 ± 0.4
late-time (Mode B)	O	1.2 ± 0.2
	H1	0.8 ± 0.3
	H2	2.6 ± 0.2
	V1	1.8 ± 0.3
	V2	3.1 ± 0.3
	V3	4.5 ± 0.7

systematic errors, are summarized in table 5 and graphically illustrated in figure 9. Using these rates and correcting for differences in the time constant and capture rates between 0.25% Gd-loaded scintillator and 0.1% Gd-loaded water, it is possible to estimate the expected beam-induced neutron background rates for ANNIE Phase-II.

10 Systematic uncertainties in the beam-induced neutron event rate

10.1 Systematic uncertainties on N_n

The largest systematic uncertainty on the raw neutron count N_n arises from the CIT background subtraction. We have two independent estimates of the CIT background at every position except V4 (where only Mode A data are available). For positions other than V4 and O, the pre-beam estimate of the CIT background rate (see section 8.1.1) is taken to be identical to the most shielded position (O) and is thus likely to be an underestimate. The post-beam method, on the other hand, has the potential to overestimate the CIT background due to beam contamination. Table 6 summarizes the CIT event rates obtained with both methods. We see that for the inner positions (O, V1, and H1) the post-beam CIT background estimate is consistent with the position O pre-beam estimate. For the positions closer to the edge and top of the tank, the differences between the post-beam and position O pre-beam estimate noticeably increase, leading them to dominate the systematic uncertainty. As described in section 8.3, we estimate the final CIT background count at each position (N_n^{CIT}) and its statistical uncertainty using a statistically weighted mean of the two measurements and its standard error. Treating the two measurements as belonging to a simple random sample (of size two) allows one to compute a sample standard deviation

$$\mathrm{SD}(N_n^{\mathrm{CIT}}) = \left[\frac{w_{\mathrm{pre}} \, (N_n^{\mathrm{pre}} - N_n^{\mathrm{CIT}})^2 + w_{\mathrm{post}} \, (N_n^{\mathrm{post}} - N_n^{\mathrm{CIT}})^2}{w_{\mathrm{pre}} + w_{\mathrm{post}} - (w_{\mathrm{pre}}^2 + w_{\mathrm{post}}^2)/(w_{\mathrm{pre}} + w_{\mathrm{post}})} \right]^{1/2} \tag{10.1}$$

which we take as the systematic error.

2020 JINST 15 P03011

A second source of systematic uncertainty is contamination from neutrons produced by beam neutrino interactions in the water tank. These lead to signal events for the planned Phase-II physics measurement, but in the context of Phase-I, they represent a source of background for the measurement of beam-correlated sky-shine and dirt neutrons. However, because only about 1% of beam spills are expected to produce a neutrino interaction in the tank, the contribution of these events to the measured Phase-I neutron rates can be no more than about 4×10^{-4} neutrons / m^3 / spill. This value is small compared to the measured rates at all NCV positions (see table 5) except position O, where it is still small compared to the estimated uncertainties. We therefore neglect the contribution of these neutrons in the Phase-I analysis.

The systematic uncertainty on the after-pulsing subtraction is small and has been neglected. Because of this the systematic errors on N_n are identical to those on N_n^{CIT} and have been omitted in table 5.

10.2 Measurement of ϵ_{NCV} and associated systematic error

To determine the final measured value of the NCV efficiency, we adopt the same general approach that was used to combine two independent measurements of the CIT neutron candidate event rate (see sections 8.3 and 10.1). In this case, the two measurements of interest are the NCV efficiency calibrations performed with a ^{252}Cf source (section 7.1) and with cosmic-ray muons (section 7.2). The NCV efficiency and its statistical error are calculated using a statistically weighted mean of the two measurements and its standard error. The reciprocal of each measurement's statistical variance is used as a weighting factor. As in section 10.1, we treat the two efficiency measurements as forming a simple random sample, and we take the sample standard deviation as an estimate of the systematic uncertainty. The combined measurement of the NCV efficiency is thus given by

$$\epsilon_{\mathrm{NCV}} = 10.5 \pm 0.5_{\mathrm{stat}} \pm 2.3_{\mathrm{syst}}\%. \tag{10.2}$$

10.3 Systematic uncertainties in exposure and volume scaling

For the uncertainty on beam exposure $\mathcal{P}$, we adopt the 2% systematic uncertainty found during routine calibrations of the beam current toroids [9]. We also adopt uncorrelated uncertainties of 1.27 cm for the NCV vessel's outer dimensions and 0.16 cm for its wall thickness, leading to a relative uncertainty on the NCV liquid volume V_{NCV} of 5.7%.

10.4 Combined uncertainty estimate

The combined statistical and systematic uncertainty on the beam-induced neutron event rate $\mathcal{R}^{\mathrm{NCV}}$ at each position is derived by analytically propagating both the statistical and the previously described systematic uncertainties. The uncertainties on the factors $\frac{\Delta t^{\mathrm{ROI}}}{\Delta t^{\mathrm{pre}}}$, $\frac{\Delta t^{\mathrm{ROI}}}{\Delta t^{\mathrm{post}}}$ and $\frac{\mathcal{T}}{\mathcal{T}_{\mathrm{O}}}$ (used to estimate the CIT background) are negligible and therefore omitted. The resulting systematic uncertainties appear in the last column of table 5.

11 Implications for the ANNIE neutron multiplicity measurement

We can predict both the dominant source and expected rate of beam-correlated background neutrons for the ANNIE Phase-II physics program. Table 5 shows that the background event rate observed

2020 JINST 15 P03011

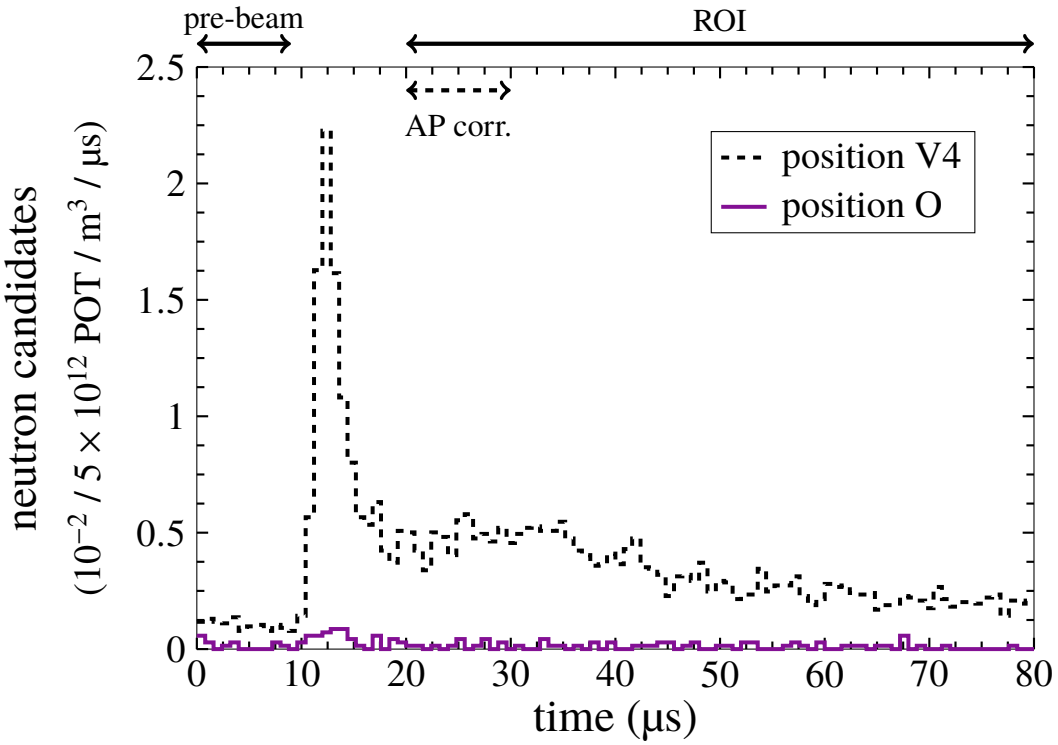

Figure 8. Time distributions of the neutron event rates measured at NCV position V4 (top of the tank, dashed black) and at position O (center of the tank, solid purple). In the DAQ Mode A data shown here, the neutrino beam arrives at 10 μs. At the top of the plot, the time intervals used to measure beam-correlated neutron captures ("ROI") and the constant-in-time background ("pre-beam") are indicated with solid lines. A dashed interval ("AP corr.") is also used to mark the early portion of the ROI in which a correction for after-pulsing is applied in the analysis (see section 8.2).

at the top center of the tank (i.e., position V4) is significantly larger than at all other positions, including the most upstream location, H2. This result is consistent with the beam-induced neutron background being dominated by sky-shine rather than dirt neutrons, and it qualitatively agrees with previous SciBooNE results that showed a large excess of events near the top of the detector briefly after the beam crossing [6]. The rapid fall-off of the background event rate over just 15 cm of depth is consistent with a soft neutron energy spectrum.

In order to ensure efficient containment of final-state neutrons, the Phase-II measurement will select only events with neutrino interaction vertices in a small (~2.5 m^3) fiducial region vertically centered in the tank and slightly upstream of the tank center in the beam direction. The full water volume will be doped with a 0.1% concentration by mass of dissolved Gd. Neutron capture candidates will be accepted anywhere in the ~14 m^3 active volume bounded by the tank PMTs.

The dashed line on the inset of figure 9 shows which NCV positions are located within the active detection volume of the ANNIE Phase-II detector. The active region will be located from 36 cm below the water line (at the top) to 353.5 cm below the water line (at the bottom). Similarly, the octagonal footprint of the inner region of the detector will be 20.3 cm away from the wall of the tank at the octagon corners and as far as 27.2 cm at the midpoint of each side. The highest

2020 JINST 15 P03011

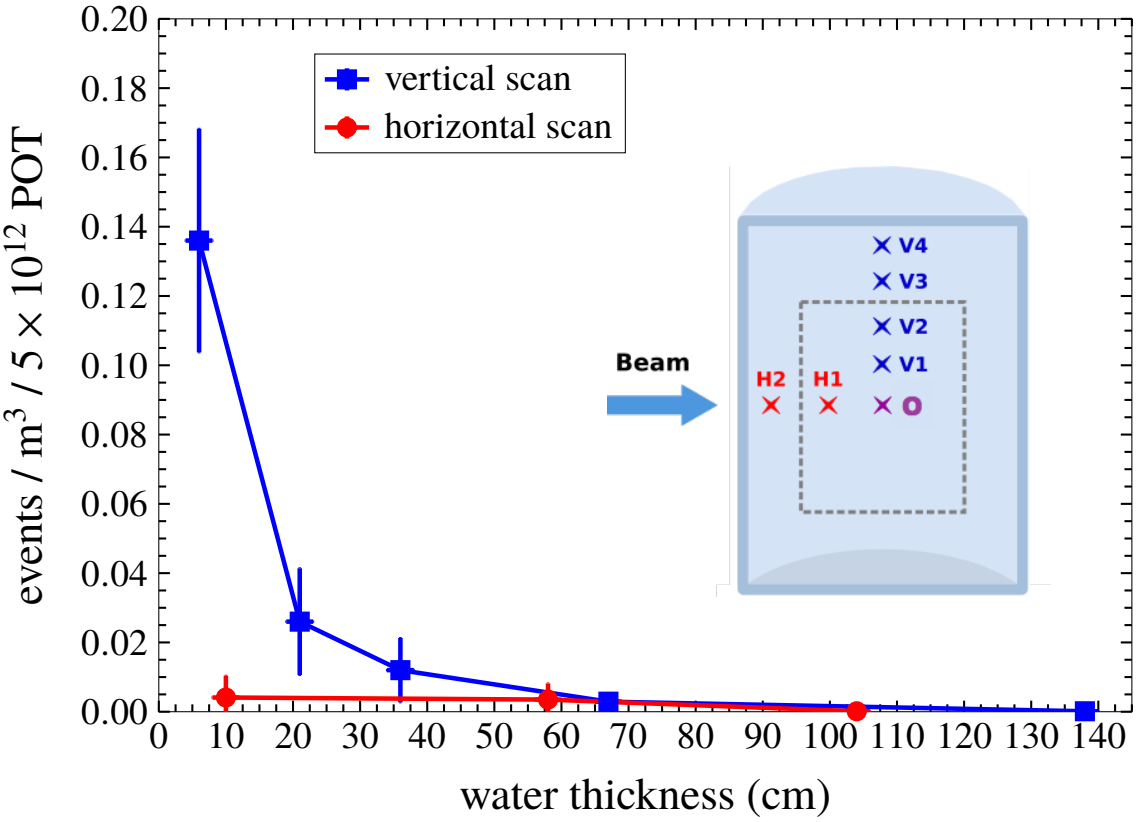

Figure 9. Beam-correlated neutron candidate event rates measured during ANNIE Phase-I. For the blue square data points, the "water thickness" reported on the horizontal axis is the depth of the water above the top of the NCV. For the red circle data points, it is the smallest distance between the side of the tube forming the NCV vessel and the beam side of the tank. The inset diagram shows the NCV positions included in the red and blue datasets. Position O (the center of the tank) is shown in purple to indicate that it is included in both the red and blue data. The dashed line indicates which NCV positions are contained within the active region of ANNIE Phase-II. Error bars shown in the plot include both statistical and systematic contributions.

beam-induced background neutron rate within this active volume was measured at position V2 to be 0.012 neutrons per m^3 per spill. This rate continued to drop with depth until position O where it is consistent with zero within errors.

The ANNIE Phase-II detector is expected to see an average of about one charged-current neutrino interaction per ~150 BNB spills. Since neutrino interactions and background neutrons are statistically independent, the per-spill neutron rate can be thought of as the probability of detecting a background neutron following a signal neutrino interaction in Phase-II.

Using the estimated background rates within the expected 14-m^3 active volume of ANNIE Phase-II, it is possible to place an upper bound on the contribution of the beam-induced neutron background to ANNIE signal events. The projections given here are highly conservative and rely on two assumptions. First, the rates along the horizontal scan are assumed to be radially symmetric. This assumption is likely accurate for any side-penetrating neutrons that originate from sky-shine. The dirt-neutron rates would, if anything, be lower on the downstream side of the tank. Second, we

2020 JINST 15 P03011

take the background rates below 138 cm of water to be constant and consistent with those measured along the horizontal scan at 138 cm depth (positions O, H1 and H2).

With these assumptions, we integrate the interpolated rates over the 14-m^3 active volume to obtain an estimated average rate of $\mathcal{R}_{\mathrm{n}}^{\mathrm{tank}} = 0.053\,^{+0.053}_{-0.025}\,^{\mathrm{stat+syst}}$ beam-correlated background neutrons per ANNIE Phase-II signal event. This is nearly an order of magnitude below the expected 0.42 primary neutrons per charged-current neutrino interaction derived from GENIE simulations.

To account for correlations between NCV positions when assessing the uncertainty on $\mathcal{R}_{\mathrm{n}}^{\mathrm{tank}}$, we relied on Monte Carlo simulations. In a set of five hundred thousand trials, N_n for each NCV position was varied about its measured value based on the statistical and systematic uncertainties for each term in eq. (8.3). With the exception of $N_n^{10\ \mu\mathrm{s}}$ and N_n^{later}, which were treated as Poisson random variables, all other quantities were varied by sampling corrections from a normal distribution with mean zero and standard deviation equal to the quoted uncertainty of interest. The NCV detection efficiency ϵ_{NCV}, total exposure $\mathcal{P}$, and NCV volume V_{NCV} were likewise varied about their central values for each trial, but the same factors were used at all NCV positions. Unphysical negative rates were set to zero during each trial in agreement with the "method of sensitivity limit" proposed by Lokhov and Tkachov [30]. One-sigma errors on $\mathcal{R}_{\mathrm{n}}^{\mathrm{tank}}$ were obtained by computing empirical 68.27% confidence intervals using the results from the Monte Carlo trials.

There are two considerations that will bias our estimate of $\mathcal{R}_{\mathrm{n}}^{\mathrm{tank}}$ slightly high relative to the true neutron background in Phase-II. The first is that the shielding effect from Gd-loaded water (where thermal neutrons have a shortened diffusion length) is likely to be slightly higher than the measured shielding effect from the pure water volume in Phase-I. The second is that the neutron capture time in the Gd-loaded scintillator of the NCV is shorter than that in Gd-loaded water. This means that the Phase-I signal window will capture slightly more background neutrons (which have a higher probability of coming in at late times relative to the beam) relative to the same window in Phase-II. We can therefore confidently say that the beam-induced neutron background in ANNIE Phase-II will be acceptably low.

12 Conclusions

In this paper we present an estimate of neutron backgrounds derived from measurements in the Neutron Capture Volume of the ANNIE Phase-I detector. Quantifying the size of these backgrounds is important in establishing the feasibility of the ANNIE Phase-II physics program.

Neutron backgrounds are highest at the top of the tank at a rate of $0.136 \pm 0.009_{\mathrm{stat}} \pm 0.031_{\mathrm{syst}}$ per cubic meter per spill. These backgrounds drop off rapidly with depth to be consistent with zero for most of the inner volume. With all of our assumptions erring on the side of overestimating these backgrounds, we still obtain an event rate of $\mathcal{R}_{\mathrm{n}}^{\mathrm{tank}} = 0.053\,^{+0.053}_{-0.025}\,^{\mathrm{stat+syst}}$ beam-induced background neutrons per neutrino interaction in ANNIE Phase-II. Comparing this result with a GENIE prediction of 0.42 neutrons per charged-current neutrino interaction in ANNIE allows us to conclude that the beam-correlated background neutron rate is acceptably low for the Phase-II physics measurements.

The position dependence of these backgrounds is consistent with a flux of low-energy sky-shine neutrons, mostly at the top of the tank, that drops off rapidly with depth. Optically isolating the active volume of the ANNIE Phase-II detector 36 cm below the top of the water line and 20 cm from the side will suffice to reduce these backgrounds to an acceptable rate.

2020 JINST 15 P03011

The results presented in this paper are relevant to other BNB experiments such as SBND, located adjacent to ANNIE Hall, where dirt neutrons and sky-shine could present similar backgrounds. The techniques described in this paper will also be applicable to any future water-based near detectors, especially those with Gd-loading or water-based liquid scintillators. The operational experience gained during Phase-I has informed the design of ANNIE Phase-II.

Acknowledgments

This work could not have been accomplished without the support, personnel, facilities, and resources of Fermi National Accelerator Laboratory. The collaboration owes a special thanks to James Kilmer and the rest of the engineering staff for their guidance in the design and mechanical aspects of the detector. John Voirin and his technical staff were essential in the deployment and staging of this experiment. Geoffrey Savage and Michael Cherry provided critical guidance and assistance in the process of designing, certifying, and deploying our readout electronics. A special thanks to Yau Wah at the University of Chicago for his generous loan of the K0TO readout boards used in the data acquisition system. The ANNIE collaboration would like to dedicate the success of this effort to the memory of William "Bill" Lee, our experimental liaison who served as a guide, mentor, and friend to so many of our collaborators. The activities of the ANNIE experiment are supported by the U.S. Department of Energy, Office of Science, Office of High Energy Physics under contracts DE-SC0016326 and DE-SC0019214, together with the Science and Technology Facilities Council and the Scottish Universities Physics Alliance (United Kingdom). JF Beacom is supported by NSF Grant PHY-1714479. M Wetstein is supported by DE-SC0017946 and his startup fund at Iowa State. M. Sanchez, F. Krenrich, and A. Weinstein are supported by DE-SC0015684. M. Sanchez would like to acknowledge her support under NSF-1056262 and M. Wetstein acknowledges support through the McCormick Fellowship at U. Chicago for much of the early work that lead to the proposal of the ANNIE experiment. V. Fischer and S. Gardiner are supported by the DOE National Nuclear Security Administration through the Nuclear Science and Security Consortium under award number DE-NA0003180.

References

[1] I. Stancu et al., *Technical Design Report for the* 8 *GeV Beam*, Fermi National Accelerator Laboratory, FERMILAB-DESIGN-2001-03 (2001).

[2] ANNIE collaboration, *Accelerator Neutrino Neutron Interaction Experiment (ANNIE): Preliminary Results and Physics Phase Proposal*, arXiv:1707.08222.

[3] J.F. Beacom and M.R. Vagins, *GADZOOKS! Anti-neutrino spectroscopy with large water Cherenkov detectors*, *Phys. Rev. Lett.* **93** (2004) 171101 [hep-ph/0309300].

[4] W.-Y. Lee et al., *Observation of the reaction* $\nu_\mu + p \to \nu_\mu + p$, *Phys. Rev. Lett.* **37** (1976) 186.

[5] B. Mukherjee, R.M. Ronningen, P. Grivins and P. Rossi, *Further evaluation of neutron skyshine dose in vicinity of the K*1200 *superconducting cyclotron of the NSCL using bubble dosimeters*, *AIP Conf. Proc.* **600** (2001) 108.

[6] H. Takei, *Identification of recoil proton tracks for a neutrino neutral-current elastic scattering cross-section measurement at SciBooNE*, http://meetings.aps.org/link/BAPS.2008.APR.D11.7 (2008).

[7] D.A. Brown et al., *ENDF/B-VIII.0: The 8th Major Release of the Nuclear Reaction Data Library with CIELO-project Cross Sections, New Standards and Thermal Scattering Data*, *Nucl. Data Sheets* **148** (2018) 1.

2020 JINST 15 P03011

[8] SciBooNE collaboration, *The SciBooNE Experiment at FNAL*, *Nucl. Phys. Proc. Suppl.* **188** (2009) 182.

[9] MiniBooNE collaboration, *The Neutrino Flux prediction at MiniBooNE*, *Phys. Rev.* **D 79** (2009) 072002 [arXiv:0806.1449].

[10] Eljen Technology, *Gadolinium Loaded EJ-331, EJ-335*, https://eljentechnology.com/images/products/data_sheets/EJ-331_EJ-335.pdf (2016).

[11] CDF collaboration, *Scintillation counters for the CDF muon upgrade*, *Int. J. Mod. Phys.* **A 16** (2001) 1139.

[12] SciBooNE collaboration, *Search for Charged Current Coherent Pion Production on Carbon in a Few-GeV Neutrino Beam*, *Phys. Rev.* **D 78** (2008) 112004 [arXiv:0811.0369].

[13] C. Andreopoulos et al., *The GENIE Neutrino Monte Carlo Generator*, *Nucl. Instrum. Meth.* **A 614** (2010) 87 [arXiv:0905.2517].

[14] Y. Sugiyama et al., *The Data Acquisition System for the KOTO Experiment*, *IEEE Trans. Nucl. Sci.* **62** (2015) 1115 [arXiv:1406.3907].

[15] B. Richards and J. Eisch, *ANNIEDAQ Phase 1*, 10.5281/zenodo.1489338 (2018).

[16] B. Richards, *ToolDAQ Framework v2.1.1*, 10.5281/zenodo.1482767 (2018).

[17] B. Richards et al., *ToolAnalysis Phase1*, 10.5281/zenodo.1489983 (2018).

[18] F. Neves et al., *ZE3RA: The ZEPLIN-III Reduction and Analysis Package*, 2011 *JINST* **6** P11004 [arXiv:1106.0808].

[19] M.-M. Bé et al., *Table of Radionuclides*, vol. 4 of *Monographie BIPM-5*, Bureau International des Poids et Mesures, Pavillon de Breteuil, F-92310 Sèvres, France (2008).

[20] T.E. Valentine, *Evaluation of prompt fission gamma rays for use in simulating nuclear safeguard measurements*, *Ann. Nucl. Energy* **28** (2001) 191.

[21] Saint-Gobain Crystals, *LYSO scintillation material*, https://www.crystals.saint-gobain.com/sites/imdf.crystals.com/files/documents/lyso-material-data-sheet.pdf (2018).

[22] T.J. Roberts and D.M. Kaplan, *G4beamline simulation program for matter-dominated beamlines*, in *Proceedings of the 2007 IEEE Particle Accelerator Conference (PAC)*, pp. 3468–3470 (2007) [DOI].

[23] S. Seibert et al., *RAT (is an Analysis Tool) User's Guide*, http://rat.readthedocs.io/en/latest/ (2014).

[24] J. Kremer et al., *Measurements of ground-level muons at two geomagnetic locations*, *Phys. Rev. Lett.* **83** (1999) 4241.

[25] R. Brun and F. Rademakers, *ROOT: An object oriented data analysis framework*, *Nucl. Instrum. Meth.* **A 389** (1997) 81.

[26] F. James and M. Winkler, *MINUIT User's Guide*, http://seal.web.cern.ch/seal/documents/minuit/mnusersguide.pdf (2004).

[27] J. Verbeke, J. Randrup and R. Vogt, *Fission Reaction Event Yield Algorithm FREYA 2.0.2*, *Comp. Phys. Comm.* **222** (2018) 263.

[28] J. Verbeke, J. Randrup and R. Vogt, *Fission Reaction Yield Algorithm FREYA 2.0.2 user manual*, Tech. Rep. LLNL-SM-705798, Lawrence Livermore National Laboratory (2016).

[29] GEANT4 collaboration, *GEANT4: A Simulation toolkit*, *Nucl. Instrum. Meth.* **A 506** (2003) 250.

[30] A.V. Lokhov and F.V. Tkachov, *Confidence intervals with a priori parameter bounds*, *Phys. Part. Nucl.* **46** (2015) 347 [arXiv:1403.5429].

2020 JINST 15 P03011